IEEE Access
Multidisciplinary ⋮ Rapid Review ⋮ Open Access Journal

Received May 14, 2022, accepted May 31, 2022, date of publication June 10, 2022, date of current version June 15, 2022.

Digital Object Identifier 10.1109/ACCESS.2022.3182108

Low-Profile Wideband Solar-Cell-Integrated Circularly Polarized CubeSat Antenna for the Internet of Space Things

HEESU WANG, (Graduate Student Member, IEEE), YONG BAE PARK, (Senior Member, IEEE), AND IKMO PARK, (Member, IEEE)
Department of Electrical and Computer Engineering, Ajou University, Suwon 16499, South Korea

Corresponding author: Ikmo Park (ipark@ajou.ac.kr)

This work was supported in part by the National Research Foundation of Korea (NRF) Grant through the Korea Government [Ministry of Science and ICT (MSIT)] under Grant NRF-2022R1F1A1065324 and Grant 2021R1A4A1030775, and in part by the Basic Science Research Program through the National Research Foundation of Korea (NRF) funded by the Ministry of Science and ICT under Grant 2020R1A2B5B01002251.

ABSTRACT This paper proposes a low-profile wideband circularly polarized (CP) antenna using solar cell patches as radiation elements and a sequentially rotated feeding network for CubeSat applications. To realize a wide axial ratio (AR) bandwidth with a compact size, a sequentially rotated feeding network was designed by modifying a quadrature hybrid coupler and a rat-race coupler that has a small change in phase difference even when the frequency changes. A wideband CP patch array antenna was designed by combining a C-shaped slot-coupled solar cell patch in conjunction with a novel feeding network. The overall size of the proposed CP CubeSat antenna is $100 \times 100 \times 7.2$ mm^3 ($0.83\ \lambda_o \times 0.83\ \lambda_o \times 0.06\ \lambda_o$ at 2.5 GHz). Solar cells occupy 79% of the antenna area, enabling efficient energy harvesting. The −10 dB impedance bandwidth is 1.98–3.0 GHz, which is a fractional bandwidth of approximately 41.0%. The 3-dB AR and 3-dB gain bandwidths are 1.98–3.0 GHz (41.0%) and 1.82–2.98 GHz (46.6%), respectively. The proposed CP solar patch array antenna demonstrates a constant radiation pattern within the −10 dB impedance bandwidth. The proposed CubeSat antenna is suitable for use in an Internet of Space Things (IoST) autonomous communication system.

INDEX TERMS Circularly polarized antenna, CubeSat antenna, hybrid coupler, Internet of Space Things, S-band antenna, sequentially rotated antenna, solar cell integrated antenna.

I. INTRODUCTION

The *Internet of Things* (IoT) refers to things or people connected through a network, so they can effectively exchange information through an embedded communication system. The IoT is recognized as a key driving force for 5G/6G wireless communication due to its ubiquitous characteristics, which can operate anytime and anywhere, as well as its application-oriented operation, which can connect numerous physical points [1]. It is expected that more than 70 billion devices will be connected by 2025, which poses many challenges to the practical realization of the IoT. Therefore, countries around the world are seeking the evolution of a hyper-connected society based on IoT technology [1]–[3].

The associate editor coordinating the review of this manuscript and approving it for publication was Tutku Karacolak.

In line with this trend, various types of IoT devices are being developed. With the rapid increase of wide-area IoT and short-range IoT, the number of devices connected to the network is expected to increase explosively in the future. Currently, connectivity for IoT solutions is realized through a variety of terrestrial networks, including but not limited to wireless personal area networks and low-power wide-area networks. However, there are still many areas where it is difficult to provide coverage due to financial problems, complex environments, and rugged terrain. To this end, the concept of the Internet of Space, which utilizes Low Earth Orbit satellites as a possible solution, has been proposed. The *Internet of Space Things* (IoST) is a system that enables mobile communication anywhere in the world using low-orbit satellites located at altitudes of 160 to 2,000 km, as shown in Fig. 1 [4]. The rapidly changing IoT environment makes it difficult to

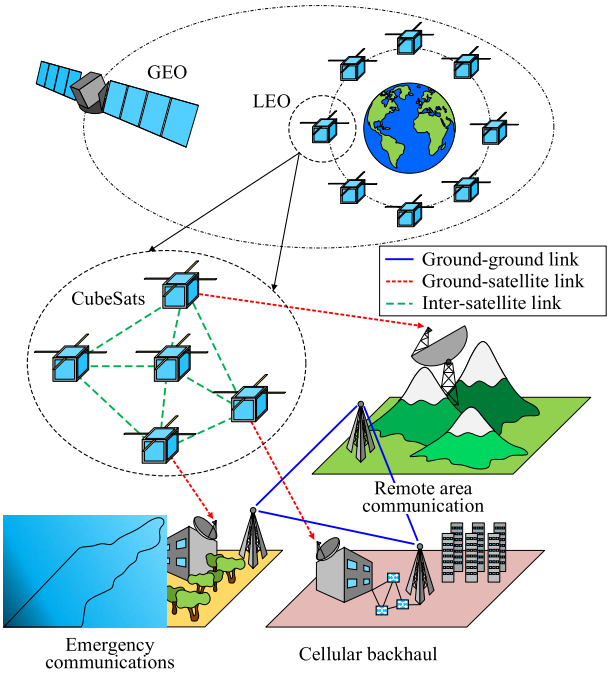

FIGURE 1. Conceptual diagram of the Internet of Space Things (IoST).

implement global satellite communication based on existing medium and large satellites requiring a long development schedule and high development costs. Considering the shortcomings of existing medium and large satellites, a new type of small satellite called CubeSat is actively being developed to implement a new IoST [5], [6].

A *CubeSat* is a cubic-shaped standardized small satellite weighing less than 1.33 kg with dimensions of 10 cm × 10 cm × 10 cm, defined as 1 U [7], [8]. A CubeSat can be used alone or in groups of multiple units. CubeSats have the advantage of greatly reducing costs because commercial off-the-shelf components are extensively used, and the development and distribution cycle is very short because standardized devices are implemented. In addition, CubeSat orbits can respond much more actively to satellite disturbances because the number of CubeSats used in orbit is large [7]. A CubeSat is very small, and many components must share limited space. Consequently, the antenna of CubeSat must be efficiently utilized within a small area. A solar cell is used as the power source for CubeSat; many studies on solar-cell-integrated antennas are being conducted to efficiently utilize the restricted surface area of CubeSat [9]. A solar cell-integrated antenna using a transparent electrode was proposed [10]–[12]. An antenna using a transparent electrode, such as indium tin oxide (ITO), has a simple design. However, ITO is expensive and results in low antenna efficiency due to the low conductivity of thin conductors. An antenna structure combining a slot with a solar cell was proposed [13]–[15]. The structure in which the slots are arranged between the gaps of the solar cell array is also simple in design. However, it is difficult to change the antenna's structure for optimal performance [13]. An antenna with a slot inserted by cutting the solar cell's structure can be designed into various shapes. Therefore, it is easy to obtain the desired antenna characteristics. However, the amount of output current collected by the solar cell decreases because the area of the solar cell is reduced by the presence of the slot [14]. Antennas using solar cells as metasurfaces have been proposed [16], [17]. A metasurface antenna can realize high gains and wide bandwidths. However, as the operating frequency increases, the size of the solar cell used as the metasurface unit cell becomes very small. Therefore, connecting each solar cell for direct current collection is complicated. An antenna using solar cells as a patch, proposed in [18]–[20], is simple in design and can achieve high gains and wide bandwidths. In addition, the efficiency of the solar cell is not reduced, and the solar cell's energy harvest is easy. However, to design a solar cell patch antenna with a wide bandwidth, the overall size of the antenna must be increased.

Circularly polarized (CP) antennas are widely used as satellite antennas because they are less affected by the installation direction of the transmitting and receiving antennas, the multipath effect, and the Faraday effect in the ionosphere [21]–[26]. Many kinds of research have investigated the design of CP antennas [27]–[39]. The sequentially rotated feeding network is widely used as a feeding structure for CP antennas because of its small size and simple structure [27]–[33]. However, the conventional sequentially rotated feeding network has low isolation between output ports. This narrows the axial ratio (AR) bandwidth of the antenna. The phase difference between the output ports changes as the frequency varies, thus changing the antenna's radiation pattern. To realize a wide AR bandwidth and a constant radiation pattern, a sequentially rotated feeding network using a phase circuit, such as a Schiffman phase shifter, has been presented [34]–[38]. The sequentially rotated feeding network using the Schiffman phase-shifter displays a small phase difference between the output ports over a wide frequency range, and the AR bandwidth is wide due to the high isolation between output ports. However, the Schiffman phase-shifter requires a Wilkinson power divider to improve the isolation at the expense of power loss. In addition, the Schiffman phase shifter consists of long transmission lines, which causes the Schiffman phase shifter to be very large. This, in turn, limits its application to a small antenna feeding structure. In [39], a sequentially rotated feeding network using a branch-line coupler was put forward. The branch-line coupler has high isolation and little change in the phase difference between output ports over a wide frequency range. In addition, the branch-line coupler can be easily miniaturized by bending the transmission lines of the coupler. Thus, it is easy to use in the antenna's feeding structure.

In this paper, we propose a CP antenna with low-profile, high-gain, wideband characteristics using a solar cell patch as the radiating element and a sequentially rotated feeding network implemented with a modified branch-line coupler for use in CubeSat. The proposed antenna has a wide bandwidth and little variation in its radiation pattern. In addition,

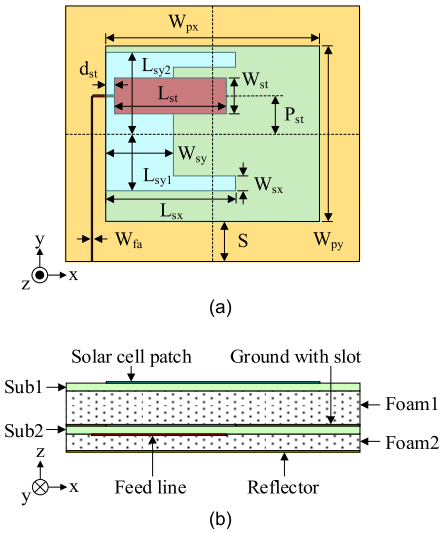

FIGURE 2. Geometry of the single antenna: (a) top view and (b) side view.

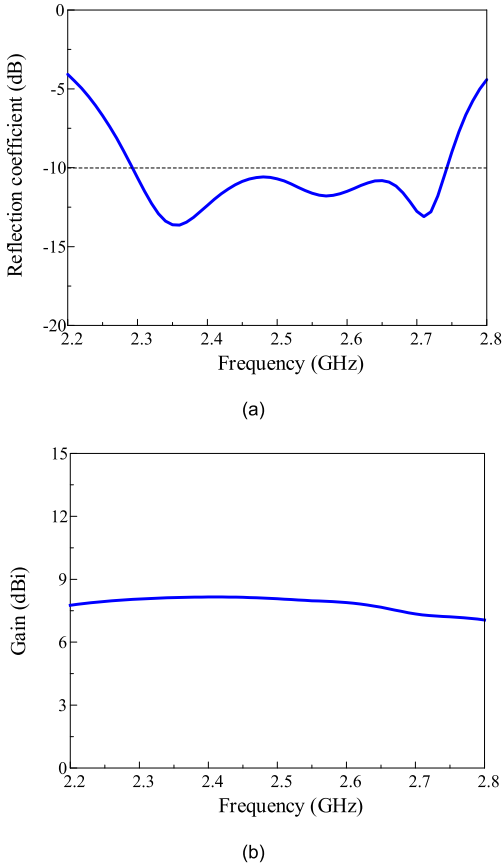

FIGURE 3. Characteristics of the single antenna: (a) reflection coefficient and (b) gain.

by using a solar cell as the radiating element and placing it on CubeSat's surface, the efficiency of the solar cell is not reduced, and solar cell energy harvesting is simple because few solar cells are used.

II. WIDEBAND PATCH ANTENNA

An aperture-coupled patch antenna has a wider impedance bandwidth than a microstrip line-fed patch antenna. Energy

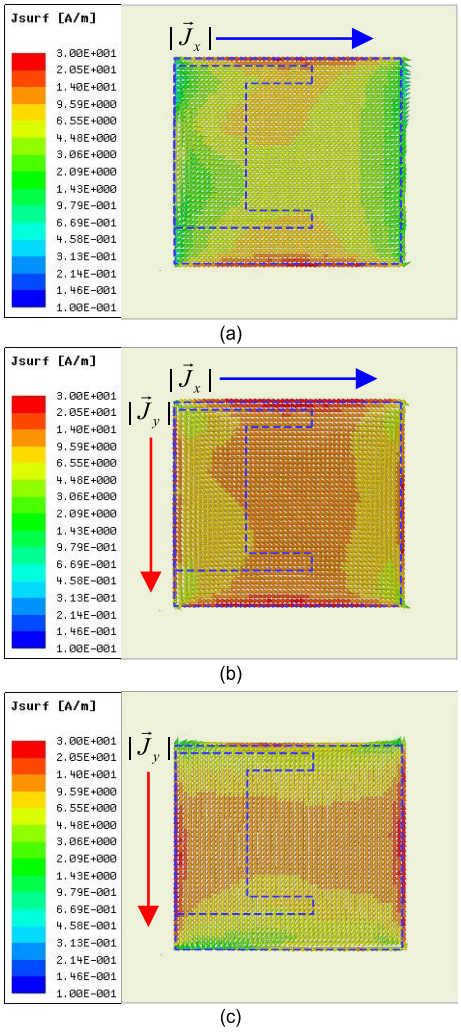

FIGURE 4. Current distribution on the solar cell patch: (a) 2.37 GHz, (b) 2.56 GHz, and (c) 2.71 GHz.

harvesting is simple when solar cells are used as a patch because the patch and feeding structure are not directly connected. Due to these advantages, a wideband patch antenna was designed using the aperture-coupled method.

A. C-SHAPE SLOT-COUPLED SOLAR CELL INTEGRATED PATCH ANTENNA

A single patch antenna with low-profile and broadband characteristics was first designed. The substrate used for the antenna design was a ROGERS RO4003C ($\varepsilon_r = 3.38$, $\tan\delta = 0.0027$). The thickness of the substrate was 0.508 mm. Fig. 2 shows the structure of the single-patch antenna. The antenna consists of substrates 1 and 2, a reflector to reduce back radiation, and foams 1 and 2 to support the antenna structure. A rectangular silicon solar cell patch was placed on top of substrate 1. Foam 1 is inserted between substrates 1 and 2 to support both substrates. The ground plane and slot are printed on the top side of substrate 2. Instead of the conventional straight, narrow slot, a C-shaped wide slot with good impedance matching performance was used [40].

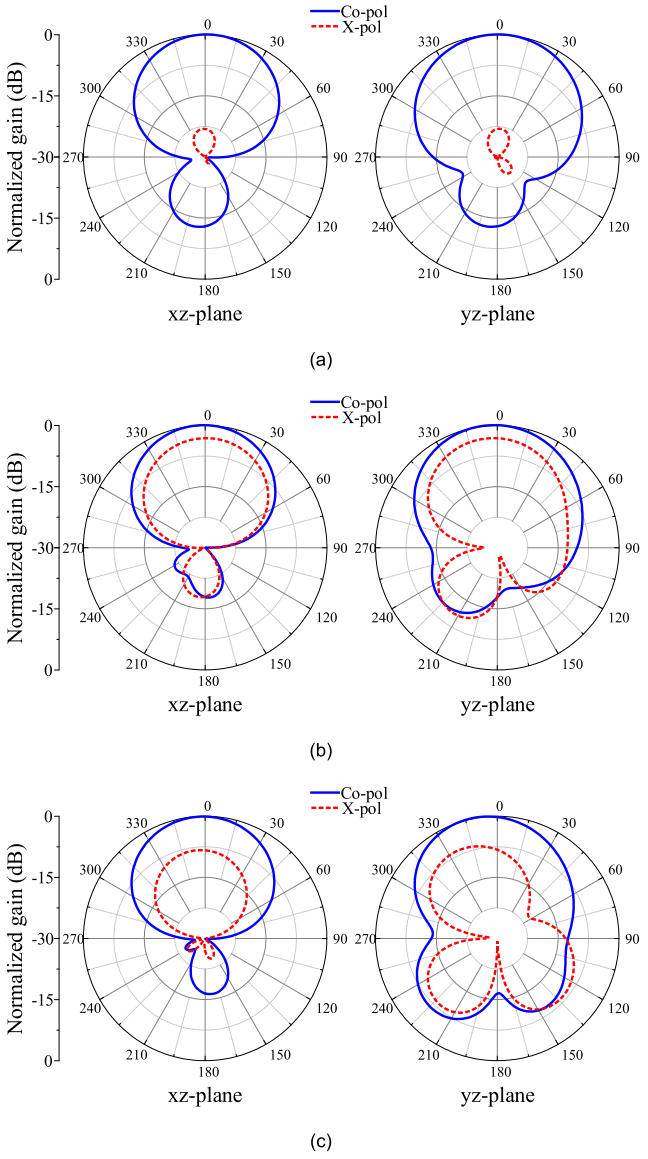

FIGURE 5. Radiation patterns of the single antenna at: (a) 2.37 GHz, (b) 2.56 GHz, and (c) 2.71 GHz.

The microstrip line and the tuning stub of the antenna are printed on the bottom side of substrate 2. A thin microstrip line with a width W_{fa} is a transmission line connecting a single patch antenna and a feeding network, and a wide strip line with a width W_{st} is a tuning stub for a single patch antenna. The tuning stub with a wide line width has less impedance change in a wide frequency range; thus, a wider impedance bandwidth can be realized [41]. The impedance bandwidth was further widened by generating modes with varying polarization directions by adjusting the positions of the slots and feed lines [42]. A reflector is placed at the bottom of the antenna to reduce back radiation, and foam 2 is inserted between substrate 2 and the reflector to support substrate 2. The design and analysis of the antenna were performed using the ANSYS High-Frequency Structure Simulator (HFSS). The design parameters of the single patch

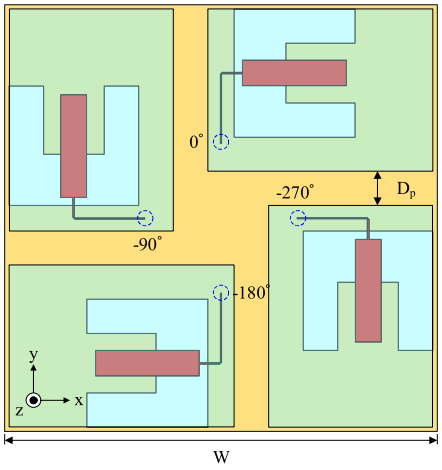

FIGURE 6. Geometry of the 2 × 2 circularly polarized array antenna.

antenna are as follows: $W_{px} = 46$ mm, $W_{py} = 42$ mm, $S = 10$ mm, $W_{st} = 8$ mm, $L_{st} = 26$ mm, $d_{st} = 0$ mm, $P_{st} = 8$ mm, $W_{fa} = 0.3$ mm, $W_{sx} = 2$ mm, $L_{sx} = 27$ mm, $W_{sy} = 16$ mm, $L_{sy1} = 12$ mm, $L_{sy2} = 20$ mm, $h_1 = h_3 = 0.508$ mm, $h_2 = 4.5$ mm, and $h_4 = 1.5$ mm.

Fig. 3 illustrates the characteristics of the single patch antenna. Fig. 3(a) presents the reflection coefficient of the antenna. The −10 dB impedance bandwidth of the single antenna is 2.27–2.74 GHz, which is a fractional bandwidth of 18.8%. Fig. 3(b) presents the gain of the antenna. The peak gain of the single-patch antenna is 8.0 dBi, and the 3-dB gain bandwidth is 1.97–3.00 GHz, a fractional bandwidth of 41.4%. Fig. 4 shows the surface current distribution of the antenna. At the first resonance frequency of 2.37 GHz, the current flowing in the patch and the direction of polarization are in the x-axis direction. At the second resonance frequency of 2.56 GHz, the current flows in both the x- and y-axis directions of the patch. Thus, there are two polarization components. At the highest resonance frequency of 2.71 GHz, the current flows in the y-axis direction of the patch.

Fig. 5 reveals the antenna radiation patterns at 2.36 GHz, 2.56 GHz, and 2.71 GHz. At 2.56 GHz, cross-polarization is high because the current flows in the x-axis and y-axis directions. At 2.36 GHz and 2.71 GHz, cross-polarization is low because the current flows only in one direction.

B. 2 × 2 CIRCULARLY POLARIZED ARRAY WITH WIDEBAND PATCH ANTENNA

A 2 × 2 CP array antenna using the designed single patch antenna was implemented, and its characteristics were demonstrated. After arranging the four patch antennas in a given 10 cm × 10 cm space, a phase difference of 90° was set for each antenna to achieve circular polarization. When the array antenna was designed using four single-patch antennas, the characteristics of the single antenna changed. ANSYS HFSS was used to optimize the array antenna. Fig. 6 depicts an optimized 2 × 2 CP array antenna. The design parameters of the optimized array antenna are as follows: W = 100 mm,

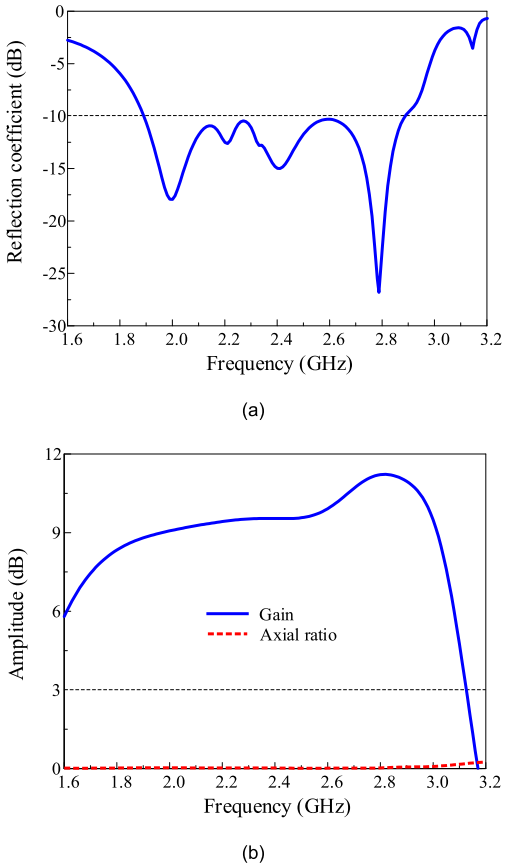

FIGURE 7. Characteristics of the 2 × 2 circularly polarized array antenna: (a) reflection coefficient and (b) gain and axial ratio.

$W_{px} = 52$ mm, $W_{py} = 38$ mm, $D_p = 8$ mm, $W_{st} = 8$ mm, $L_{st} = 25$ mm, $d_{st} = 0$ mm, $P_{st} = 4$ mm, $W_{fa} = 0.3$ mm, $W_{sx} = 8$ mm, $L_{sx} = 28$ mm, $W_{sy} = 10$ mm, $L_{sy1} = 11$ mm, $L_{sy2} = 19$ mm, $h_1 = h_3 = 0.508$ mm, $h_2 = 4.5$ mm, and $h_4 = 1.5$ mm.

Fig. 7 shows the characteristics of the array antenna. Fig. 7(a) demonstrates the reflection coefficient of the antenna. The −10 dB impedance bandwidth of the array antenna is 1.89–2.89 GHz, which is a fractional bandwidth of 41.8%. The −10 dB impedance bandwidth of the array antenna is wider than that of a single antenna. Fig. 7(b) shows the antenna gain and AR. The single-patch antenna has a problem in which the cross-polarization level increases and the polarization direction changes as the frequency increases. However, the gain and AR are not affected when the single patch antennas are configured as a CP array antenna.

III. SEQUENTIALLY ROTATED FEEDING NETWORK

To realize a CP antenna with a wide AR bandwidth and little change in the radiation pattern even with frequency changes, a sequentially rotated feeding network consisting of modified branch-line couplers with a small size and wideband characteristics is used.

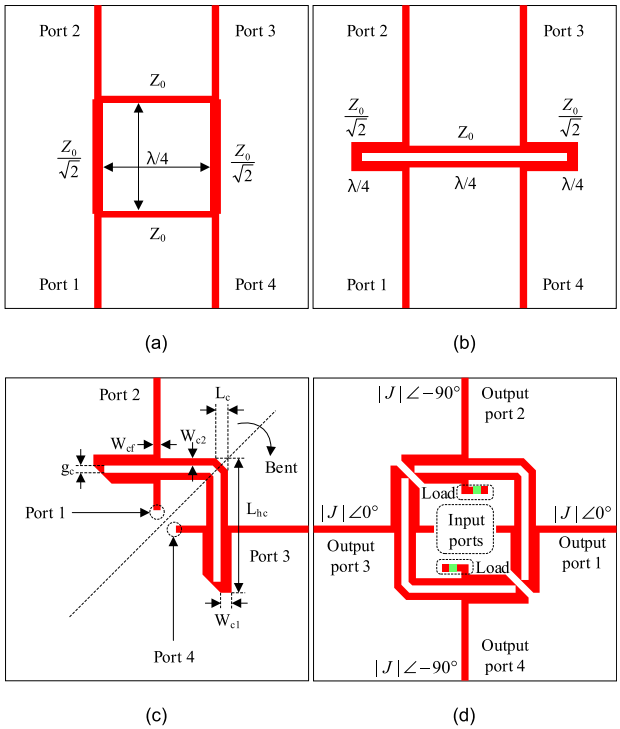

FIGURE 8. Geometry of the modified quadrature hybrid coupler: (a) conventional coupler, (b) folded coupler, (c) proposed coupler, and (d) feeding network using two proposed couplers.

A. MODIFIED QUADRATURE HYBRID COUPLER

Fig. 8 shows a modified quadrature hybrid coupler designed with 100-Ω input and output ports. By modifying the quadrature hybrid coupler, the area occupied by the transmission line is greatly reduced [39]. Fig. 8(a) is a diagram of a conventional quadrature hybrid coupler with a large circuit area, limiting its use as an antenna-feeding structure. Fig. 8(b) is a diagram of a quadrature hybrid coupler in which the empty space inside the circuit is reduced by folding the transmission line with 0.707 Z_o characteristic impedance. Fig. 8(c) is a schematic of the modified quadrature hybrid coupler with reduced spacing achieved by bending the conventional quadrature hybrid coupler 90°. The proposed modified quadrature hybrid coupler has a much smaller circuit area than the conventional coupler. Fig. 8(d) illustrates a feeding structure with two input ports and four output ports designed using two modified quadrature hybrid couplers. Load resistors are connected to the isolated port of each coupler.

When power with the same phase is supplied to two input ports, the phase of the output power of output ports 1 through 4 is 0°, 90°, 0°, and 90°, respectively. The design parameters of the modified quadrature hybrid coupler are as follows: $L_{hc} = 19.2$ mm, $W_{c1} = 1.15$ mm, $W_{c2} = 0.75$ mm, $g_c = 0.25$ mm, $W_{cf} = 0.3$ mm, and $L_c = 3.0$ mm.

Fig. 9 demonstrates the characteristics of the couplers described in Fig. 8. Fig. 9(a) shows the reflection coefficient of each coupler. The −10 dB impedance bandwidth of the proposed coupler is slightly wider than that of the

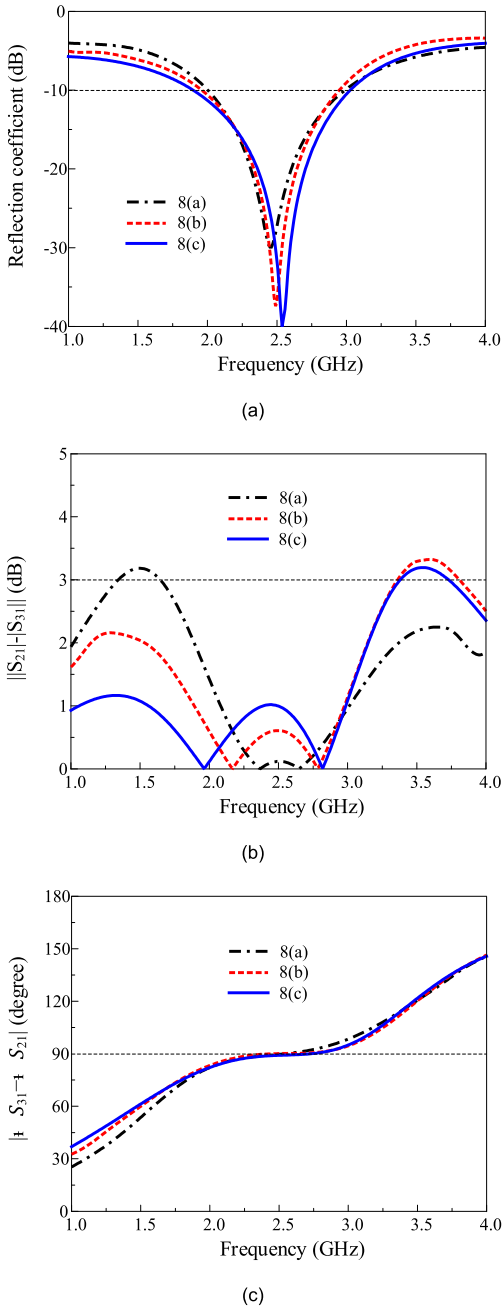

FIGURE 9. Characteristics of the quadrature hybrid couplers described in Fig. 8: (a) reflection coefficient, (b) output power amplitude difference, and (c) output power phase difference.

conventional coupler; the impedance matching is very good. Fig. 9(b) depicts the difference in output power between the output ports of the couplers. The frequency range where the power difference between the output ports of the proposed coupler is less than 2 dB is wider than that of the conventional coupler. Fig. 9(c) shows the phase difference between the output powers of the couplers. The proposed coupler shows little phase difference change over a wide frequency range. By modifying the coupler, the area that the circuit occupied is greatly reduced, and the performance is still good.

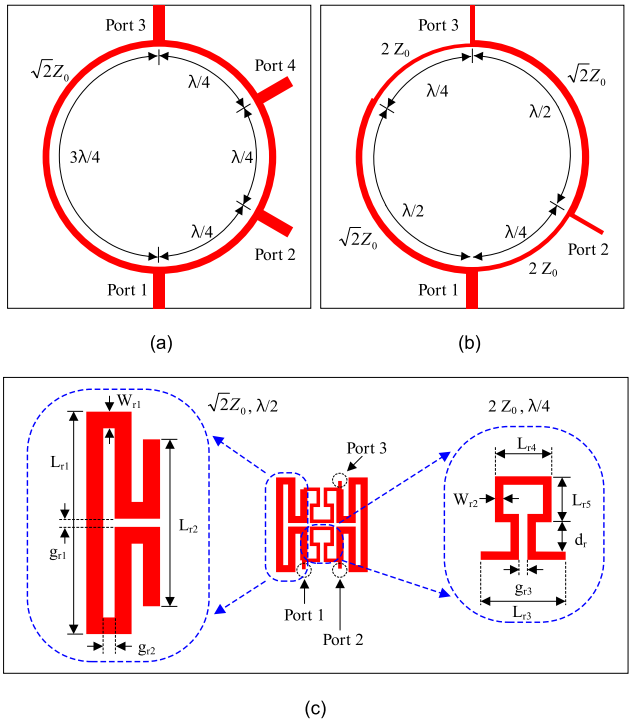

FIGURE 10. Geometry of the modified rat-race coupler: (a) conventional coupler, (b) three-port coupler with 100 Ω output port, and (c) proposed miniaturized coupler.

B. MODIFIED RAT-RACE COUPLER

An additional phase difference of 180° is required to implement circular polarization using the feeding structure in Fig. 8(d). A 180° coupler with a modified rat-race coupler was designed to implement an additional phase difference. Fig. 10(a) shows a conventional rat-race coupler. The rat-race coupler can be used as a power divider with a phase difference of 180° over a wide frequency range. However, the area occupied by the circuit is very large, and it is not suitable for use as a feeding structure for miniaturized antennas. Fig. 10(b) displays the structure in which the isolated port is removed from the conventional rat-race coupler. In the rat-race coupler, the power input to port 1 is not transmitted to port 4. Therefore, even if port 4 is removed, the rat-race coupler can be used as a power divider with a phase difference of 180°. In the proposed coupler, port 4 was removed, and the transmission line width was changed so the coupler had a 50-Ω input port and 100-Ω output ports. The coupler consists of a pair of transmission lines with a characteristic impedance of 100 Ω with a length of λ/4 and a pair of transmission lines with a characteristic impedance of 70.7 Ω with a length of λ/2. Fig. 10(c) is a modified rat-race coupler in which the size of the rat-race coupler depicted in Fig. 10(b) is reduced by folding the transmission line. In the proposed coupler, the circuit area is greatly reduced to 1/6 of the size compared with the conventional rat-race coupler. The design parameters of the modified rat-race coupler are as follows: $L_{r1} = 14.5$ mm, $L_{r2} = 12.0$ mm, $W_{r1} = 0.6$ mm, $g_{r1} = 0.6$ mm, $g_{r2} = 0.9$ mm, $L_{r3} = 6.0$ mm, $L_{r4} = 4.4$ mm, $L_{r5} = 3.05$ mm, $W_{r2} = 0.3$ mm, $g_{r3} = 0.4$ mm, and $d_r = 2.45$ mm.

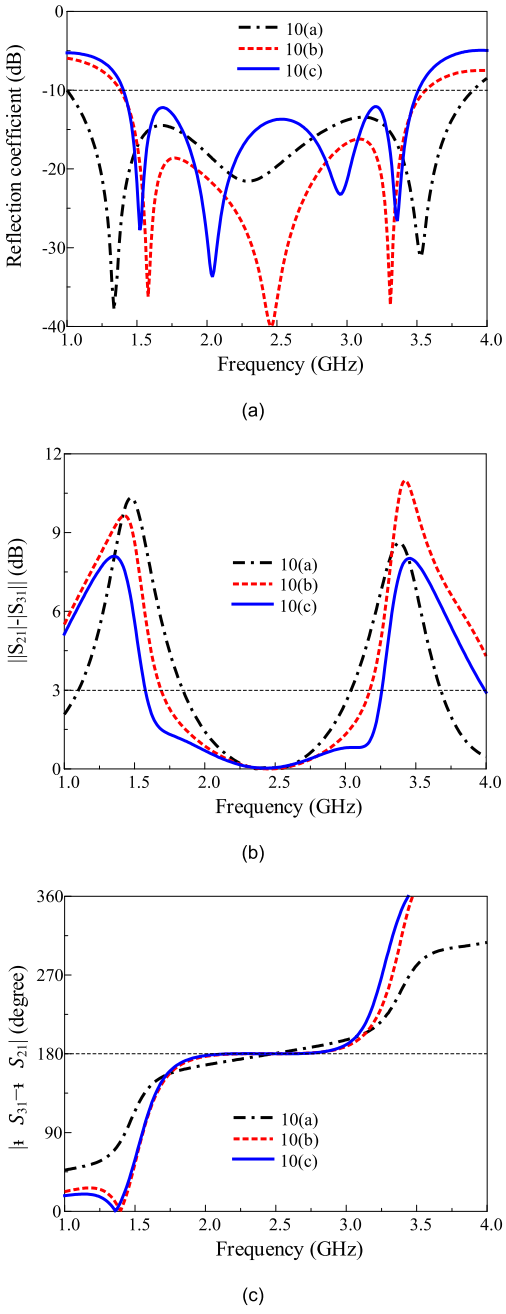

FIGURE 11. Characteristics of the rat-race couplers depicted in Fig. 10: (a) reflection coefficient, (b) output power amplitude difference, and (c) output power phase difference.

Fig. 11 displays the characteristics of the proposed rat-race couplers. Fig. 11(a) shows the reflection coefficient of the couplers depicted in Fig. 10, and Fig. 11(b) shows the output power difference of the output ports of each coupler. Fig. 11(c) demonstrates the phase difference between the output ports of each coupler.

The proposed coupler has a slightly narrower −10 dB impedance bandwidth compared to the conventional rat-race coupler. However, the output power and phase difference between the output ports are smaller than the conventional rat-race coupler within the impedance bandwidth.

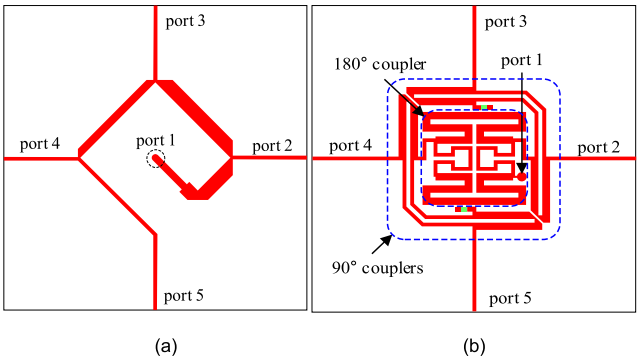

FIGURE 12. Geometry of the sequentially rotated feeding networks: (a) conventional and (b) proposed.

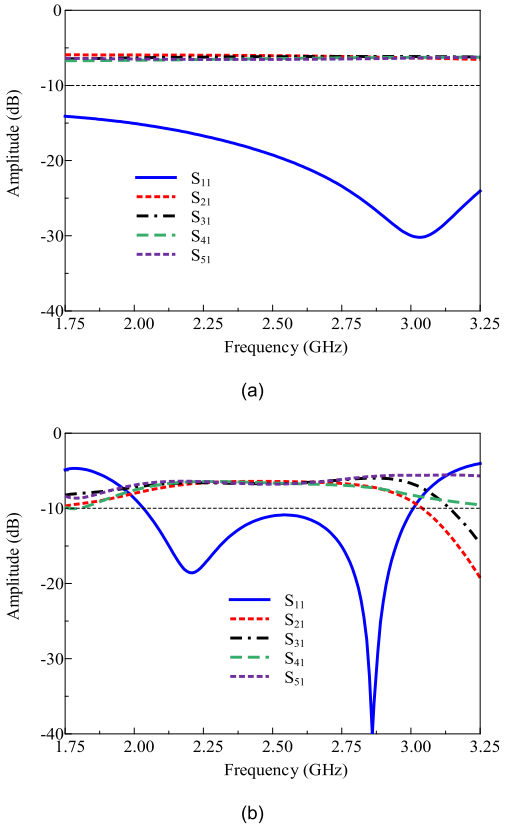

FIGURE 13. S-parameter characteristics: (a) conventional and (b) proposed.

C. PROPOSED SEQUENTIALLY ROTATED FEEDING NETWORK

By combining the previously designed modified quadrature hybrid coupler and the modified rat-race coupler, a novel sequentially rotated feeding network with one input port and four output ports was designed. Fig. 12 reveals the conventional and proposed sequentially rotated feeding networks. The area occupied by the proposed sequentially rotated feeding network is 19.9 × 19.9 mm^2, which is smaller than the area of the conventional sequentially rotated feeding network of 21 × 21 mm^2. Fig. 13 shows the amplitude characteristics of the S-parameters of the conventional and proposed

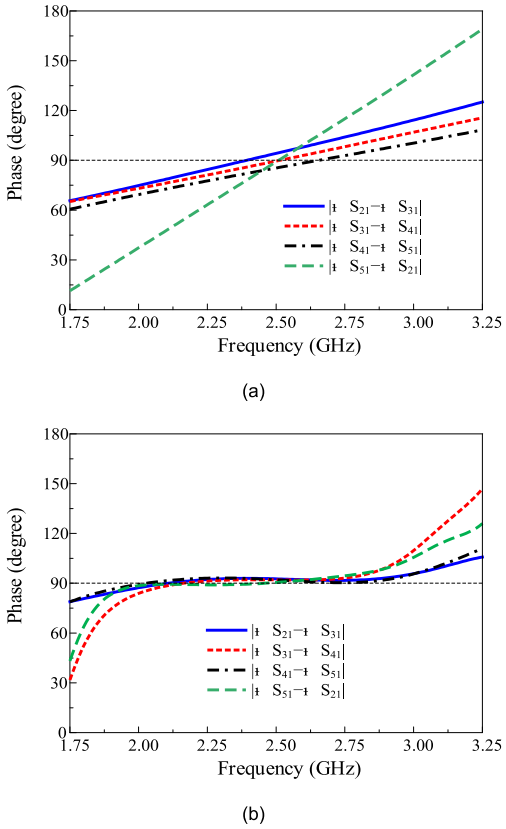

FIGURE 14. Output power phase difference characteristics: (a) conventional and (b) proposed.

feeding networks. Fig. 13(a) portrays the S-parameter of the conventional feeding network, and Fig. 13(b) shows the S-parameter of the proposed feeding network. The conventional sequentially rotated feeding network has a low reflection coefficient over a very wide frequency range, and the transmission coefficient of each output port is constant. The proposed sequentially rotated feeding network has good performance characteristics within 2.00–3.00 GHz. Fig. 14 shows the phase characteristics of the S-parameters of the conventional and proposed feeding networks. Fig. 14(a) shows the phase difference between the output ports of the conventional feeding network, and Fig. 14(b) demonstrates the phase difference between the output ports of the proposed feeding network. Because the conventional feeding network implements the phase difference based on the length of the transmission line, the electrical length of each transmission line changes at a frequency outside the center frequency, thereby changing the phase difference between the output ports. Conversely, because the proposed feeding network generates a constant phase difference over a wide frequency range, the phase difference between the output ports is stable, even at a frequency outside the center frequency.

IV. FABRICATION AND MEASUREMENT

We designed the 2 × 2 solar cell patch-integrated CP antenna by combining the proposed feeding network with the antenna

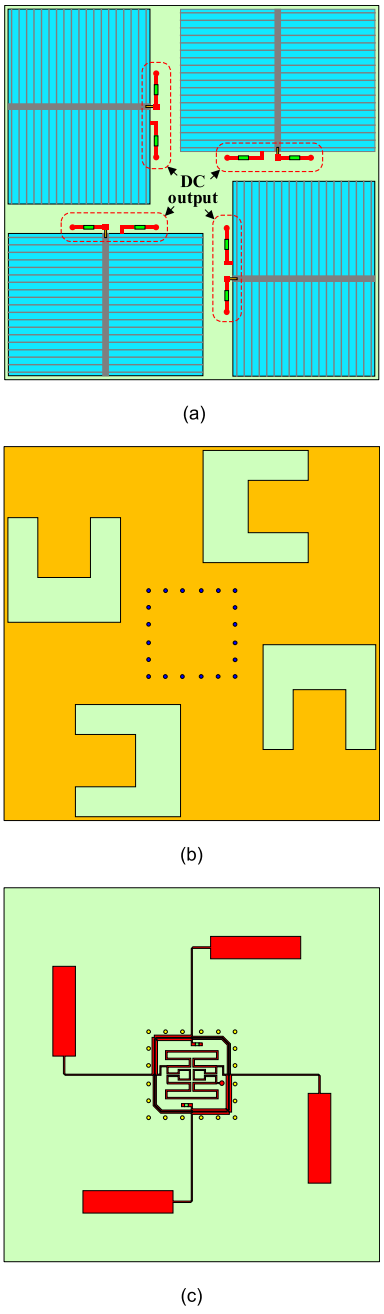

FIGURE 15. Geometry of the proposed antenna: (a) solar cell patches and RF decoupler, (b) ground plane with slots, and (c) feeding network.

designed in Section 2. Fig. 15 presents the geometry of this antenna. On the top surface of the antenna, there are four solar cell patches and a substrate supporting the solar cell, and the performance of the solar cells determines the DC performance of the antenna. Four RF decouplers, each consisting of a pair of inductors, were added for solar cell energy harvesting. One part of the RF decoupler is connected to the bottom contact of the solar cell, and the other part is connected to the grid. To implement DC energy harvesting, a pair of metal wires were connected to the end of the RF decoupler, and an inductor was used as the RF choke to

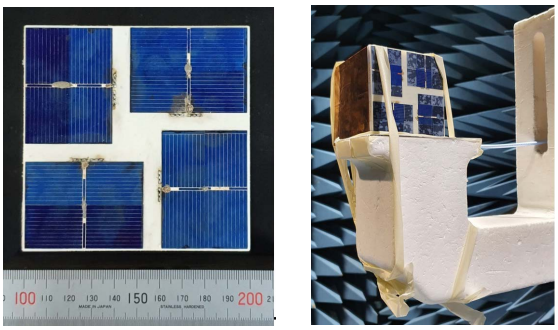

(a) (b)

FIGURE 16. Photograph of the fabricated antenna: (a) top view and (b) experimental setup.

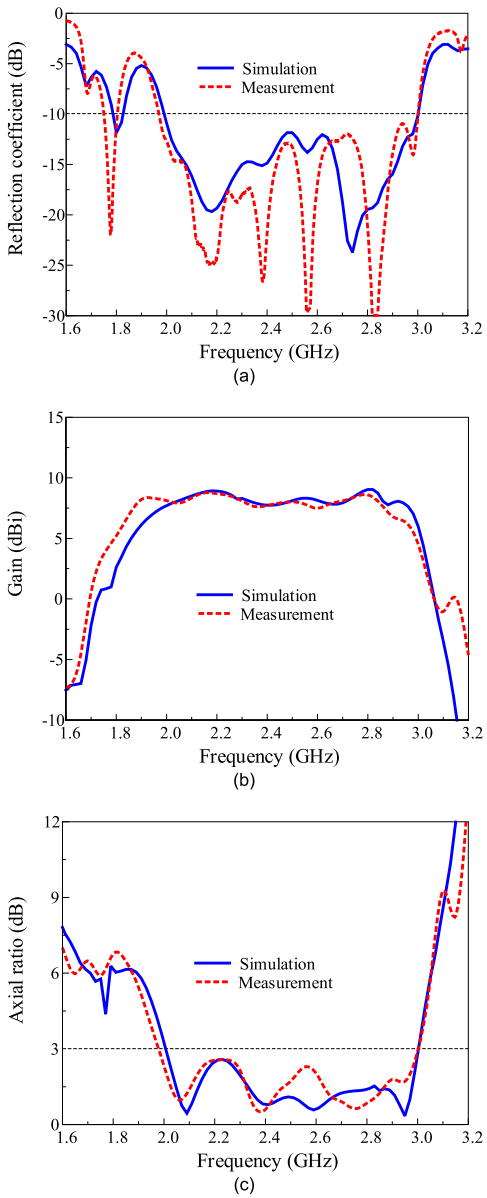

FIGURE 17. Simulated and measured results: (a) reflection coefficient, (b) gain, and (c) axial ratio.

prevent the RF signal from leaking along the wire. The middle substrate has a ground plane, including a C-shaped slot on

TABLE 1. Simulation and measurement results.

Characteristics	Simulation	Measurement
–10 dB IBW (GHz)	1.99–3.00 (40.4%)	1.98–3.00 (41.0%)
3-dB gain BW (GHz)	1.90–3.00 (44.0%)	1.82–2.98 (46.6%)
3-dB AR BW (GHz)	2.00–3.00 (40.0%)	1.98–3.00 (41.0%)
Peak gain (dBic)	9.0	8.8
RHCP HPBW		
at 2.2 GHz	56.2°/55.9°	54.0°/53.0°
at 2.5 GHz	49.7°/49.8°	52.4°/53.0°
at 2.8 GHz	44.9°/45.1°	46.9°/48.3°
(xz-/yz-plane)		

*IBW: impedance bandwidth

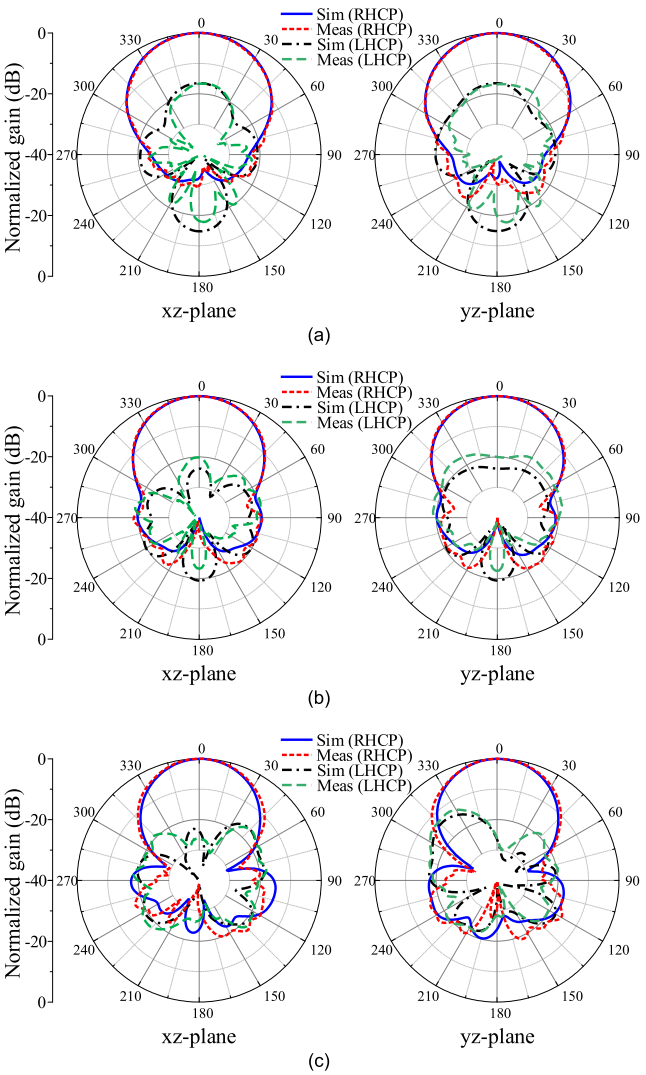

FIGURE 18. Radiation patterns at: (a) 2.2 GHz (b) 2.5 GHz, and (c) 2.8 GHz.

top, and the feeding network is printed on the bottom. The reflector is located at the bottom of the antenna. A coaxial cable was used to feed the antenna. The inner conductor of the coaxial cable is connected to the input port of the feeding network, and the outer conductor is connected to the reflector. Metal pins connect the ground plane with the reflector surrounding the feeding network, so the reflector has the same electric potential as the ground plane.

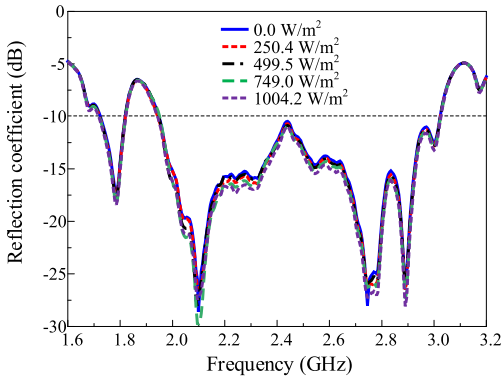

FIGURE 19. Measured reflection coefficient of the proposed antenna with different light intensity values.

The designed antenna was fabricated, and its performance was measured. Fig. 16 shows the fabricated antenna. A Rohde & Schwarz ZVA 67 vector network analyzer was used to measure the antenna reflection coefficient, and the antenna radiation pattern was measured in the MTG anechoic chamber. Fig. 17 displays the simulated and measured antenna characteristics. The measured result of the −10 dB impedance bandwidth of the antenna is 1.98–3.0 GHz, a fractional bandwidth of 41%. The 3-dB gain bandwidth and AR bandwidth are 1.82–2.98 GHz and 1.98–3.0 GHz, respectively, which are fractional bandwidths of 46.6% and 41.0%, respectively. The measured results are very similar to the simulation results. Fig. 18 shows the antenna radiation patterns at 2.2 GHz, 2.5 GHz, and 2.8 GHz. The simulated and measured antenna gains at 2.2 GHz are 8.5 dBic and 8.7 dBic, respectively. The simulated and measured gains at 2.5 GHz are 8.4 dBic and 8.1 dBic, respectively, and the simulated and measured gains at 2.8 GHz are the same at 8.8 dBic. In the proposed antenna, the radiation patterns of the antenna do not change significantly, even when the frequency changes, and the radiation patterns in the xz- and yz-planes are very symmetrical. The simulation and measurement results of the antenna are summarized in Table 1.

V. EFFECTS OF THE SOLARCELL ON ANTENNA PERFORMANCE

The electrical properties of a solar cell are greatly affected by the amount of incident light. When a solar cell is exposed to light, the electrical conductivity of the solar cell increases significantly [43]. A change in the electrical conductivity of a solar cell may affect the characteristics of the antenna. Fig. 19 shows the measured reflection coefficient of the antenna with different light intensity values. To validate the effect of light intensity, the reflection coefficient was measured under light intensities of 0.0, 250.4, 499.5, 749.0, and 999.4 W/m^2 (with a 100 W halogen lamp). As shown in Fig. 19, the measured reflection coefficient differs slightly depending on the light intensity values. However, the shape of the curves in the figure is almost identical, indicating that the light intensity has little effect on the reflection coefficient of the antenna.

VI. COMPARISON

The proposed antenna was compared with other solar cell-integrated antennas. The solar cell-integrated CP antenna presented in [10] consists of a transparent electrode radiation element and a conventional sequentially rotated feed network. The electrical size of the antenna is 3.33 × 3.33 × 0.66 λ_o^3, and the −10 dB impedance bandwidth is over 30%. The 3-dB gain bandwidth is approximately 16.3%, and the AR bandwidth is approximately 20%. The peak gain is 17 dBic. However, the gain and AR bandwidths are narrow, and the antenna is very large. The solar cell-integrated microstrip slot array antenna presented in [13] used a slot antenna as a radiation element and implemented CP using a sequentially rotated feed network. The electrical size of the antenna is 2.71 × 2.71 × 0.001 λ_o^3. The −10 dB impedance, 3-dB gain, and 3-dB AR bandwidths are over 17.3%. However, the peak gain is only 6.6 dBic, a very low gain compared to its large size. In [17], a CP patch antenna with a solar cell metasurface is presented. The electrical size of the antenna is 0.87 × 0.87 × 0.076 λ_o^3, and the −10 dB impedance bandwidth is 19.1%. The 3-dB gain bandwidth is approximately 33%, and the AR bandwidth is about 16.1%. The peak gain is 8.8 dBic. Although the gain was high compared to the size, the metasurface composed of solar cells requires many inductors for energy harvesting and is difficult to implement. A CP antenna using a solar cell patch antenna and a quadrature hybrid coupler is presented in [18]. The electrical size of the antenna is 0.67 × 1.14 × 0.016 λ_o^3, and the −10 dB impedance bandwidth is 12.5%. The peak gain of this antenna is almost 6 dBic. However, the 3-dB gain and AR bandwidths are very narrow. A low-profile solar cell-integrated patch antenna is proposed in [18]. The electrical size of the antenna is 1.6 × 1.2 × 0.024 λ_o^3. The −10 dB impedance bandwidth and 3-dB gain bandwidths are 15.5% and 21.3%, respectively. This antenna has a peak gain of 9.4 dBi, which is low compared to the size of the antenna. It also has a low form factor of 55.4%. A solar cell patch antenna with two aperture-coupled feeds is presented in [20]. The electrical size of the antenna is 1.31 × 1.31 × 0.060 λ_o^3. The −10 dB impedance bandwidth and 3-dB gain bandwidth are very narrow, at 6.8% and 8.4%, respectively. This antenna has a high peak gain of 10.8 dBi, with a low form factor of 45%.

The antenna proposed in this paper has an electrical size of 0.83 × 0.83 × 0.06 λ_o^3, a −10 dB impedance bandwidth of 41.0%, and a 3-dB gain and AR bandwidths of 46.6% and 41.0%, respectively. In addition, the solar cell occupies 79% of the antenna area. Thus, it has a higher form factor compared with that of conventional CP solar cell-integrated antennas ([13]: 73.5%, [17]: 56.3%, [18]: 79.0%, [19]: 55.4%, [20]: 45.0%). Here, the form factor is defined as the ratio of the total area utilized by the solar cell for energy harvesting to the given surface area of the antenna. Hence, it has superior performance characteristics compared to conventional solar cell-integrated antennas. In addition, there is no problem with the beam tilt due to changes in frequency. The performance

TABLE 2. Performance comparison of the antenna in different configurations.

Antenna structure	Size (λ_o^3)	Technology used	–10 dB IBW (%)	3-dB AR BW (%)	3-dB gain BW (%)	Peak gain (dBic)	Form factor (%)
Ref. [10]	3.33 × 3.33 × 0.66	ITO-copper	>30	20.0	16.3	17	N/A*
Ref. [13]	2.71 × 2.71 × 0.001	Microstrip slot array	> 17.3	> 17.3	> 17.3	6.6	73.5
Ref. [17]	0.87 × 0.87 × 0.076	Solar cell metasurface	19.1	16.1	33	9.0	56.3
Ref. [18]	0.60 × 1.14 × 0.016	Solar cell patch	12.5	N/A	N/A	5.96	79.0
Ref. [19]	1.6 × 1.2 × 0.024	Solar cell patch	15.5	Not CP	21.3	9.4	55.4
Ref. [20]	1.31 × 1.31 × 0.060	Solar cell patch	6.8	Not CP	8.4	10.8	45.0
Proposed	0.83 × 0.83 × 0.060	Solar cell patch	41.0	41.0	46.6	8.8	79.0

*Solar cell size not provided. IBW: impedance bandwidth.

characteristics of the conventional antennas and the proposed antenna are summarized in Table 2.

VII. CONCLUSION

In this paper, we propose a 2 × 2 sequentially rotated CP array antenna that combines a solar cell patch antenna having wideband characteristics with a novel sequentially rotated feeding network that boasts a stable phase difference over a wide frequency range. The proposed antenna has wide gain and AR bandwidths, and the radiation pattern is stable even when the frequency changes. The electrical size of the proposed antenna at the center frequency of 2.5 GHz is $0.83 \times 0.83 \times 0.06\ \lambda_o^3$. The −10 dB impedance bandwidth is 1.98–3.00 GHz. The 3-dB gain bandwidth and AR bandwidth are 1.82–2.98 GHz and 1.98–3.0 GHz, respectively. Moreover, the proposed antenna has a high form factor of 79%. Due to these advantages, the proposed antenna is suitable not only for CubeSats but also for other satellite applications. Therefore, it is useful for implementing an IoST autonomous communication system.

REFERENCES

[1] L. Chettri and R. Bera, "A comprehensive survey on Internet of Things (IoT) toward 5G wireless systems," *IEEE Internet Things J.*, vol. 7, no. 1, pp. 16–32, Jan. 2020.

[2] S. N. R. Kantareddy, I. Mathews, R. Bhattacharyya, I. M. Peters, T. Buonassisi, and S. E. Sarma, "Long range battery-less PV-powered RFID tag sensors," *IEEE Internet Things J.*, vol. 6, no. 4, pp. 6989–6996, Aug. 2019.

[3] *Visual Networking Index: Global Mobile Data Traffic Forecast Update 2017–2022 White Paper*, Cisco, San Jose, CA, USA, Feb. 2019.

[4] I. F. Akyildiz and A. Kak, "The Internet of Space Things/CubeSats: A ubiquitous cyber-physical system for the connected world," *Comput. Netw.*, vol. 150, pp. 134–149, Feb. 2019.

[5] N. Saeed, A. Elzanaty, H. Almorad, H. Dahrouj, T. Y. Al-Naffouri, and M.-S. Alouini, "CubeSat communications: Recent advances and future challenges," *IEEE Commun. Surveys Tuts.*, vol. 22, no. 3, pp. 1839–1862, 3rd Quart., 2020.

[6] Y. Rahmat-Samii, V. Manohar, and J. M. Kovitz, "For satellites, think small, dream big: A review of recent antenna developments for CubeSats," *IEEE Antennas Propag. Mag.*, vol. 59, no. 2, pp. 22–30, Apr. 2017.

[7] N. Chahat, *CubeSat Antenna Design*. Piscataway, NJ, USA: IEEE Press, 2021.

[8] J. Wang, V. Manohar, and Y. Rahmat-Samii, "Enabling the Internet of Things with CubeSats: A review of representative beamsteerable antenna concepts," *IEEE Antennas Propag. Mag.*, vol. 63, no. 6, pp. 14–28, Dec. 2021.

[9] T. Yekan and R. Baktur, "Conformal integrated solar panel antennas: Two effective integration methods of antennas with solar cells," *IEEE Antennas Propag. Mag.*, vol. 59, no. 2, pp. 69–78, Apr. 2017.

[10] S. Zarbakhsh, M. Akbari, M. Farahani, A. Ghayekhloo, T. A. Denidni, and A.-R. Sebak, "Optically transparent subarray antenna based on solar panel for CubeSat application," *IEEE Trans. Antennas Propag.*, vol. 68, no. 1, pp. 319–328, Jan. 2020.

[11] W. An, L. Xiong, S. Xu, F. Yang, H.-P. Fu, and J.-G. Ma, "A Ka-band high-efficiency transparent reflectarray antenna integrated with solar cells," *IEEE Access*, vol. 6, pp. 60843–60851, 2018.

[12] T. Peter, T. A. Rahman, S. W. Cheung, R. Nilavalan, H. F. Abutarboush, and A. Vilches, "A novel transparent UWB antenna for photovoltaic solar panel integration and RF energy harvesting," *IEEE Trans. Antennas Propag.*, vol. 62, no. 4, pp. 1844–1853, Apr. 2014.

[13] Z. Zhang, B. Bai, X. Li, Y. Liu, C. Sun, and Y. Zhang, "Integration of circularly polarized microstrip slot array antenna with amorphous silicon solar cells," *IEEE Antennas Wireless Propag. Lett.*, vol. 19, no. 12, pp. 2320–2323, Dec. 2020.

[14] A. Ali, H. Wang, Y. Yun, J. Lee, and I. Park, "Compact slot antenna integrated with a photovoltaic cell," *J. Electromagn. Eng. Sci.*, vol. 20, no. 4, pp. 248–253, Oct. 2020.

[15] A. Ali, Y. Yun, H. Wang, K. Lee, J. Lee, and I. Park, "Photovoltaic cell with built-in antenna for Internet of Things applications," *IEEE Access*, vol. 9, pp. 107437–107445, 2021.

[16] S. Liu, D. Yang, Y. Chen, X. Zhang, and Y. Xiang, "Compatible integration of circularly polarized omnidirectional metasurface antenna with solar cells," *IEEE Trans. Antennas Propag.*, vol. 68, no. 5, pp. 4155–4160, May 2020.

[17] S. X. Ta, J. J. Lee, and I. Park, "Solar-cell metasurface-integrated circularly polarized antenna with 100% insolation," *IEEE Antennas Wireless Propag. Lett.*, vol. 16, pp. 2675–2678, 2017.

[18] T. R. Jones, J. P. Grey, and M. Daneshmand, "Solar panel integrated circular polarized aperture-coupled patch antenna for CubeSat applications," *IEEE Antennas Wireless Propag. Lett.*, vol. 17, no. 10, pp. 1895–1899, Oct. 2018.

[19] Y. Zhao, W. An, Y. Luo, S. Li, L. Xiong, and S. Yu, "Low-profile antenna integrated with solar cells for the 2.4 GHz band," *IEEE Antennas Wireless Propag. Lett.*, vol. 20, no. 4, pp. 443–447, Apr. 2021.

[20] Y. Luo, J. Lai, N. Yan, W. An, and K. Ma, "Integration of aperture-coupled multipoint feed patch antenna with solar cells operating at dual compressed high-order modes," *IEEE Antennas Wireless Propag. Lett.*, vol. 20, no. 8, pp. 1468–1472, Aug. 2021.

[21] S. X. Ta and I. Park, "Low-profile broadband circularly polarized patch antenna using metasurface," *IEEE Trans. Antennas Propag.*, vol. 63, no. 12, pp. 5929–5934, Dec. 2015.

[22] Z. Gan, Z.-H. Tu, Z.-M. Xie, Q.-X. Chu, and Y. Yao, "Compact wideband circularly polarized microstrip antenna array for 45 GHz application," *IEEE Trans. Antennas Propag.*, vol. 66, no. 11, pp. 6388–6392, Nov. 2018.
[23] X. Quan, R. Li, and M. M. Tentzeris, "A broadband omnidirectional circularly polarized antenna," *IEEE Trans. Antennas Propag.*, vol. 61, no. 5, pp. 2363–2370, May 2013.
[24] S. X. Ta, I. Park, and R. W. Ziolkowski, "Crossed dipole antennas: A review," *IEEE Antennas Propag. Mag.*, vol. 57, no. 5, pp. 107–122, Oct. 2015.
[25] J. Chen, C. Jin, B. Zhang, and Z. Shen, "Combined triangle quarter-wavelength patches and their application to high-gain CP antenna," *IEEE Antennas Wireless Propag. Lett.*, vol. 19, no. 1, pp. 104–108, Jan. 2020.
[26] K. E. Kedze, H. Wang, Y. Kim, and I. Park, "Design of a reduced-size crossed-dipole antenna," *IEEE Trans. Antennas Propag.*, vol. 69, no. 2, pp. 2363–2370, Feb. 2021.
[27] C. Ma, Z.-H. Ma, and X. Zhang, "Millimeter-wave circularly polarized array antenna using substrate-integrated gap waveguide sequentially rotating phase feed," *IEEE Antennas Wireless Propag. Lett.*, vol. 18, no. 6, pp. 1124–1128, Jun. 2019.
[28] S. X. Ta and I. Park, "Compact wideband sequential-phase feed for sequentially rotated antenna arrays," *IEEE Antennas Wireless Propag. Lett.*, vol. 16, pp. 661–664, 2017.
[29] S. X. Ta and I. Park, "Compact wideband circularly polarized patch antenna array using metasurface," *IEEE Antennas Wireless Propag. Lett.*, vol. 16, pp. 1932–1936, 2017.
[30] Y.-H. Yang, J.-L. Guo, B.-H. Sun, Y.-M. Cai, and G.-N. Zhou, "The design of dual circularly polarized series-fed arrays," *IEEE Trans. Antennas Propag.*, vol. 67, no. 1, pp. 574–579, Jan. 2019.
[31] S.-K. Lin and Y.-C. Lin, "A compact sequential-phase feed using uniform transmission lines for circularly polarized sequential-rotation arrays," *IEEE Trans. Antennas Propag.*, vol. 59, no. 7, pp. 2721–2724, Jul. 2011.
[32] D. Inserra, G. Wen, and W. Hu, "Sequentially rotated circular antenna array with curved PIFA and series feed network," *IEEE Trans. Antennas Propag.*, vol. 66, no. 11, pp. 5849–5858, Nov. 2018.
[33] M. J. Veljovic and A. K. Skrivervik, "Aperture-coupled low-profile wideband patch antennas for CubeSat," *IEEE Trans. Antennas Propag.*, vol. 67, no. 5, pp. 3439–3444, May 2019.
[34] Y.-X. Guo, K.-W. Khoo, and L. C. Ong, "Wideband circularly polarized patch antenna using broadband baluns," *IEEE Trans. Antennas Propag.*, vol. 56, no. 2, pp. 319–326, Feb. 2008.
[35] L.-L. Qiu, L. Zhu, and Y. Xu, "Wideband low-profile circularly polarized patch antenna using 90° modified Schiffman phase shifter and meandering microstrip feed," *IEEE Trans. Antennas Propag.*, vol. 68, no. 7, pp. 5680–5685, Jul. 2020.
[36] Q. Liu, Z. N. Chen, Y. Liu, and C. Li, "Compact ultrawideband circularly polarized weakly coupled patch array antenna," *IEEE Trans. Antennas Propag.*, vol. 65, no. 4, pp. 2129–2134, Apr. 2017.
[37] C. Sun, "A design of compact ultrawideband circularly polarized microstrip patch antenna," *IEEE Trans. Antennas Propag.*, vol. 67, no. 9, pp. 6170–6175, Sep. 2019.
[38] W. Hu, T. Feng, S. Gao, L. Wen, Q. Luo, P. Fei, Y. Liu, and X. Yang, "Wideband circularly polarized antenna using single-arm coupled asymmetric dipoles," *IEEE Trans. Antennas Propag.*, vol. 68, no. 7, pp. 5104–5113, Jul. 2020.
[39] H. Wang and I. Park, "Compact wideband circularly polarized dipole antenna using modified quadrature hybrid couplers," *IEEE Trans. Antennas Propag.*, vol. 69, no. 12, pp. 8896–8901, Dec. 2021.
[40] S. K. Padhi, N. C. Karmakar, C. L. Law, and S. Aditya, "A dual polarized aperture coupled circular patch antenna using a C-shaped coupling slot," *IEEE Trans. Antennas Propag.*, vol. 51, no. 12, pp. 3295–3298, Dec. 2003.
[41] M. K. A. Rahim, Z. W. Low, P. J. Soh, A. Asrokin, M. H. Jamaluddin, and T. Masri, "Aperture coupled microstrip antenna with different feed sizes and aperture positions," in *Proc. Int. RF Microw. Conf.*, Sep. 2006, pp. 31–35.
[42] R. Garg, P. Bhartia, I. J. Bahl, and A. Ittipiboon, *Microstrip Patch Antenna Design Handbook*. Norwood, MA, USA: Artech House, 2001, pp. 576–579.
[43] S. V. Shynu, M. J. R. Ons, P. McEvoy, M. J. Ammann, S. J. McCormack, and B. Norton, "Integration of microstrip patch antenna with polycrystalline silicon solar cell," *IEEE Trans. Antennas Propag.*, vol. 57, no. 12, pp. 3969–3972, Dec. 2009.

HEESU WANG (Graduate Student Member, IEEE) received the B.S. and M.S. degrees in electrical and computer engineering from Ajou University, Suwon, South Korea, in 2018 and 2020, respectively, where he is currently pursuing the Ph.D. degree with the Department of Electrical and Computer Engineering. His research interests include the design of patch antennas, printed antennas, small antennas, and metasurface antennas for various wireless communication applications.

YONG BAE PARK (Senior Member, IEEE) received the B.S., M.S., and Ph.D. degrees in electrical engineering from the Korea Advanced Institute of Science and Technology, South Korea, in 1998, 2000, and 2003, respectively. From 2003 to 2006, he was at the Korea Telecom Laboratory, Seoul, South Korea. He joined the School of Electrical and Computer Engineering, Ajou University, South Korea, in 2006, where he is currently a Professor. His research interests include electromagnetic field analysis, high-frequency methods, metamaterial antennas, radomes, and stealth technology.

IKMO PARK (Member, IEEE) received the B.S. degree in electrical engineering from the State University of New York, Stony Brook, and the M.S. and Ph.D. degrees in electrical engineering from the University of Illinois at Urbana–Champaign. He joined the Department of Electrical and Computer Engineering at Ajou University, in 1996. He was at the Device and Materials Laboratory, LG Corporate Institute of Technology, Seoul, South Korea, where he had been engaged in research and development of various antennas for personal communication systems, wireless local area networks, and direct broadcasting systems. He was a Visiting Professor at the Department of Electrical and Computer Engineering, POSTECH, Pohang, South Korea, from March 2004 to February 2005, and the Department of Electrical and Computer Engineering, University of Arizona, Tucson, Arizona, USA, from July 2011 to June 2012. He has authored and coauthored over 300 technical journal and conference papers. He also holds over 50 domestic and international patents. He was the Chair of the Department of Electrical and Computer Engineering at Ajou University. He is a member of the Board of Directors with the Korea Institute of Electromagnetic Engineering and Science (KIEES). He is the Editor-in-Chief of the Proceeding of the KIEES and Journal of KIEES, the Editorial Board Member of the *International Journal of Antennas and Propagation*, and an Associate Editor of *IET Electronics Letters*. He was the Editorial Board Member of the *Journal of Electromagnetic Engineering and Science*. He is a member of Eta Kappa Nu and Tau Betta Pi.